PEG-Stabilized Core–Shell Nanoparticles: Impact of Linear *versus* Dendritic Polymer Shell Architecture on Colloidal Properties and the Reversibility of Temperature-Induced Aggregation

Torben Gillich,[†,§] Canet Acikgöz,[†,⊥] Lucio Isa,[†] A. Dieter Schlüter,[‡] Nicholas D. Spencer,[†] and Marcus Textor[†,*]

[†]Laboratory for Surface Science and Technology and [‡]Institute of Polymers, Department of Materials, ETH Zurich, Wolfgang-Pauli-Strasse 10, 8093 Zurich, Switzerland. [§]Present address: Zurich University of Applied Sciences (ZHAW), School of Engineering, Institute of Materials and Process Engineering, 8401 Winterthur, Switzerland. [⊥]Present address: OC Oerlikon Balzers AG, 9496 Balzers, Liechtenstein.

ABSTRACT Superparamagnetic iron oxide nanoparticles (SPIONs) have been widely used experimentally and also clinically tested in diverse areas of biology and medicine. Applications include magnetic resonance imaging, cell sorting, drug delivery, and hyperthermia. Physicochemical surface properties are particularly relevant in the context of achieving high colloidal nanoparticle (NP) stability and preventing agglomeration (particularly challenging in biological fluids), increasing blood circulation time, and possibly targeting specific cells or tissues through the presentation of bioligands. Traditionally, NP surfaces are sterically stabilized with hydrophilic polymeric matrices, such as dextran or linear poly(ethylene glycol) brushes. While dendrimers have found applications as drug carriers, dispersants with dendritic ("dendrons") or hyperbranched structures have been comparatively neglected despite their unique properties, such as a precisely defined molecular structure and the ability to present biofunctionalities at high density at the NP periphery. This work covers the synthesis of SPIONs and their stabilization based on poly(ethylene glycol) (PEG) and oligo(ethylene glycol) (OEG) chemistry and compares the physicochemical properties of NPs stabilized with linear and dendritic macromolecules of comparable molecular weight. The results highlight the impact of the polymeric interface architecture on solubility, colloidal stability, hydrodynamic radius, and thermoresponsive behavior. Dendron-stabilized NPs were found to provide excellent colloidal stability, despite a smaller hydrodynamic radius and lower degree of soft shell hydration compared to linear PEG analogues. Moreover, for the same grafting density and molecular weight of the stabilizers, OEG dendron-stabilized NPs show a reversible temperature-induced aggregation behavior, in contrast to the essentially irreversible aggregation and sedimentation observed for the linear PEG analogues. This new class of dendritically stabilized NPs is believed to have a potential for future biomedical and other applications, in which stability, resistance to (or reversible) aggregation, ultrasmall size (for crossing biological barriers or inclusion in responsive artificial membranes), and/or high corona density of (bio)active ligands are key.

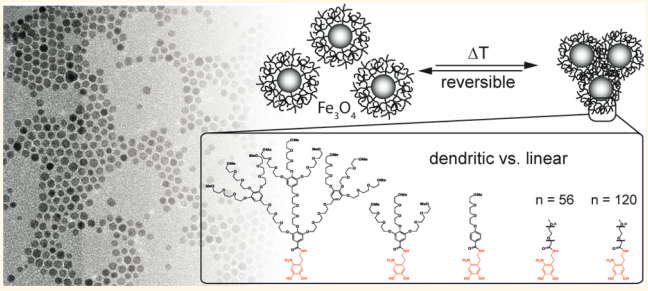

KEYWORDS: iron oxide · core–shell nanoparticles · dendron · PEG · aggregation · thermoresponsive · DLS · stability

Superparamagnetic iron oxide nanoparticles (SPIONs) are successfully used today in biomedically oriented applications such as magnetic resonance imaging (MRI, as contrast agents) and cell manipulation.[1−3] There are great expectations for additional future applications, including hyperthermia induced by external, alternating magnetic fields for cancer treatment[4] and drug delivery vehicles that can be spatially manipulated and release their cargo by means of external static and alternating magnetic fields, respectively, thus allowing for spatiotemporal control over targeted drug administration.[5,6]

For applications in which the properties of individual nanoparticles (as opposed to larger agglomerates) are to be exploited, nanoparticle stability and their degree of dispersion are key aspects. While simple electrostatic stabilization can work under specific conditions (*e.g.*, low ionic strength in the absence of macromolecules), the use of particles in biologically relevant media always requires well-engineered, (typically) polymeric

* Address correspondence to marcus.textor@mat.ethz.ch.

Received for review September 2, 2012 and accepted December 7, 2012.

Published online December 07, 2012
10.1021/nn304045q

coatings that provide steric stabilization against macromolecular adsorption (*e.g.*, by serum proteins in culture media or *in vivo*) or particle agglomeration, which can result in reduced blood circulation time and loss of function.[7,8]

A range of different methods have been proposed to stabilize and functionalize iron oxide nanoparticles.[9] In clinically used, commercially available contrast agents such as Feridex/Endorem, multiple SPIONs are typically incorporated by physical adsorption into high-molecular-weight carbohydrates (such as dextran) or synthetic polymers.[6] Disadvantages of such systems relate to the relatively poor control over cluster size and—in the context of targeting specific cells or tissue—the lack of suitable methods to introduce and present targeting ligands. An alternative approach is based on the use of lower-molecular-weight dispersants equipped with surface-active anchors, which self-assemble on the nanoparticle surface where they may form dense polymer chain layers ("brush regime"), optionally presenting functionalities for specific interactions and targeting.[10−14] Uncharged, hydrophilic and nontoxic polymers, such as dextran and poly(ethylene glycol) (PEG), have been extensively used as stabilizing agents.[15−18] The field of iron oxide particle stabilization for biomedical applications has been recently reviewed by Amstad *et al.*[9]

In comparison to linear polymers, there have been far fewer reports on the use of dendritic molecules, such as dendrimers and dendrons, for the stabilization of nanoparticles despite specific properties that make them attractive for the surface engineering of small NPs.[19−22] Indeed, despite the higher costs associated with their synthesis and purification, dendritic molecules present several advantages: (a) the structure and size of a dendron can be accurately controlled during synthesis, allowing dendrons with a perfectly defined molecular structure and weight to be prepared, due to the stepwise organic synthetic approach;[23] (b) dendritic structures are of particular interest for ultrasmall NPs with very high curvature since their radial monomer density distribution is expected to decay less rapidly with distance from the NP surface. This latter property of dendritic structures is due to their conical-like structure and focal points (Rud *et al.*, Dendritic Spherical Polymer Brushes: Self-Consistent Field Modeling, Theory and Experiment; in preparation for *Macromolecules*) and is expected to improve steric resistance to macromolecular adsorption and particle agglomeration; (c) end-group-functionalized dendritic structures have the potential for excellent and quantitatively controlled presentation of (bio)ligands at high surface densities, thanks to their perfect molecular structure, reduced flexibility of the (short) branches, and increased affinity or avidity in multivalent (bio)specific interactions, relevant in particular for biosensing applications;[24−26] (d) similar to dendrimers, small molecules such as drugs could be incorporated into the dendritic framework of dendron-stabilized NPs, making this system attractive as a potential drug release system.[27−29] (e) Stabilization of small NPs with dendrons results in dendron−NP conjugates (NP-core dendrimers or dendron-stabilized NPs) with a relatively thin organic shell and, therefore, a small size in the range of 10−30 nm.[19,22,30] This is important for biomedical applications, such as drug delivery systems, in the context of efficient cell uptake of the NPs, improved tissue diffusion,[31−34] and particularly for targeting tumors *via* the enhanced permeability and retention (EPR) effect, exploiting the nanoporous nature of blood vessels in cancerous tissue.[32,35] (f) Additionally, if adsorbed onto flat titanium oxide surfaces, oligo(ethylene glycol) (OEG)-based dendrons have shown very low protein adsorption (>99% reduction in contact with full serum compared to the bare control surfaces).[36]

While there has been work reported on the use of dendritic molecules to steer nanoparticle growth,[37−40] there are only a few studies on surface-active dendrons to disperse and stabilize ultrasmall iron oxide nanoparticles.[19,41,42] Gao *et al.*[43] and Basely *et al.*[30,44] reported on iron oxide NP surface modification by short tri- and tetra(ethylene glycol)-based dendrons of the first generation with a phosphonate at the focal point for possible application of the surface-modified particles as MRI contrast agents. Relaxivity and magnetization of the particles were studied and compared with the values of established systems. However, stability and biocompatibility upon dendronization of the particles were not investigated in detail but are key to their use in biomedical applications.

Following up on our recent publication on self-assembly of focal point oligo-catechol ethylene glycol dendrons on flat titanium oxide surfaces,[36] we report here on the stabilization of iron oxide (Fe_3O_4) NPs by dendritic and linear ethylene-glycol-based stabilizers with varying generation and chain length, respectively. In particular, differences between the linear and the dendritic PEG stabilizers with similar molecular weights will be highlighted, drawing attention to the advantages of stabilizing nanoparticles by means of dendritic surface modifiers. In contrast to our earlier work with oligo-catechol binding strategies,[36] we have used nitrocatechol as a surface anchor for the dendron, exploiting the excellent, practically irreversible binding of this anchor to iron oxide.[15,45] Particles were synthesized according to a published protocol and analyzed by means of transmission electron microscopy (TEM) and X-ray diffraction (XRD).[46] Particle stabilization was monitored by Fourier transform infrared (FT-IR) spectroscopy, thermal gravimetric analysis (TGA), dynamic light scattering (DLS), and zeta-potential measurements. DLS was also used to determine long-term colloidal particle stability in physiological buffer solution. Additionally, the thermoresponsive behavior of the stabilized particles in aqueous solutions was investigated in detail.

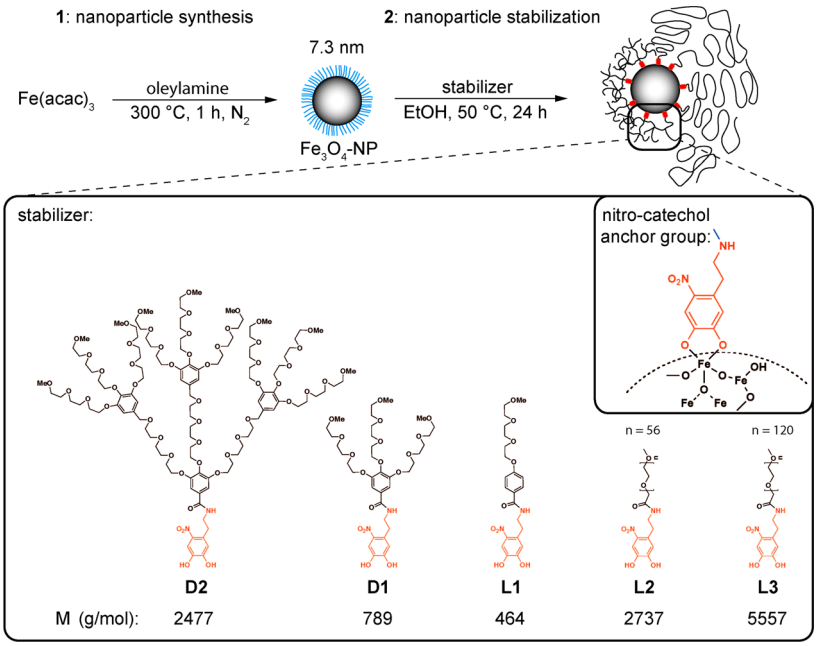

Figure 1. Illustration of NP core synthesis and stabilization with ethylene-glycol-based dispersants of linear and dendritic structure. A single nitro-catechol chelate group serves as the anchor between the macromolecular stabilizer and the iron oxide NP surface. *M* = molecular weight of the polymeric dispersants.

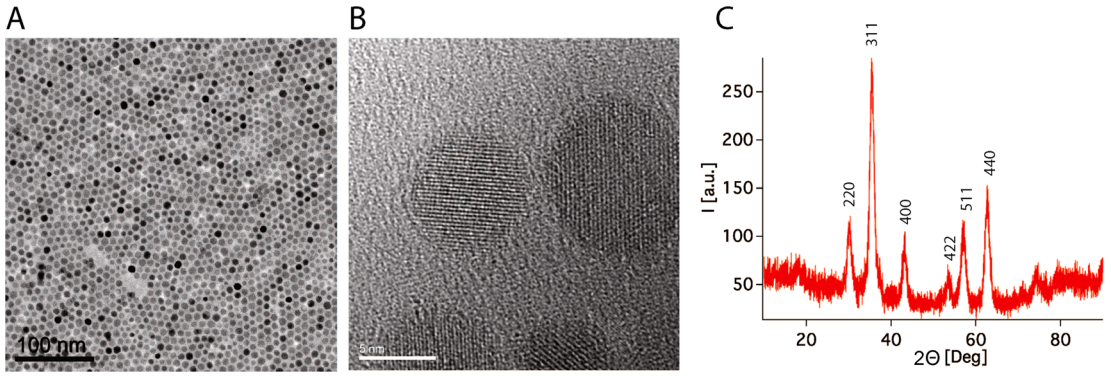

Figure 2. Iron oxide core analysis of the oleylamine-stabilized NPs (OA-NP). (A) TEM and (B) HR-TEM images. (C) XRD pattern with signal intensity *I* and diffraction angle Θ.

This work demonstrates that nitro-catechol-anchored, ethylene-glycol-based dendrons are attractive surface modifiers and stabilizers for iron oxide NPs. Additionally, fundamental interest was aroused by the demonstration that properties such as thermally induced aggregation and its reversibility, solubility, and colloidal stability are different when NPs are stabilized by dendrons or linear polymer chains.

RESULTS AND DISCUSSION

Nanoparticle Core Synthesis and Characterization. The synthesis of the core–shell iron oxide NPs and the chemical structure of the dispersants are illustrated in Figure 1.

We synthesized Fe_3O_4 NPs by a thermal decomposition procedure of iron(III) acetylacetonate ($Fe(acac)_3$ at 300 °C), according to the method published by Xu and co-workers, using oleylamine as capping agent.[46] This procedure resulted in iron oxide NPs with a mean diameter of 7.3 ± 1.2 nm (fwhm = 2.56 nm) obtained from the analysis of several thousands of NPs from TEM images (Figure 2A and Supporting Information Figure S1).

High-resolution TEM measurements provided information about the morphology and crystallinity of the particles (Figure 2B). Figure 2B demonstrates that the NPs are single crystals, that is, with only one crystalline domain per particle. The XRD pattern (Figure 2C) shows the characteristic peaks of magnetite (Figure 2C; spinel, cubic crystal system, Fe_3O_4),[16,46] which is evident despite the similarity of the diffraction patterns of magnetite and maghemite[47,48] and the presence of line broadening due to the small NP size. Line broadening can also be used to determine the mean particle diameter (size of the crystalline domain, see Materials and Methods section), which was calculated to be 6.8 ± 0.2 nm, in good agreement with the result obtained by

TABLE 1. Summary of the Physical Properties of the NPs after Oleylamine (OA, Hydrophobic) Capping and after Ligand Exchange with Ethylene-Glycol-Based Dendritic (D1 and D2) and Linear (L1, L2, and L3) Macromolecules of Different Molecular Weights, *M*[a]

NP code	water solubility	*M*(stabilizer) [g/mol]	ξ in H1 [mV]	D_z in H2 [nm]	PDI (DLS)	*m*(TGA) [wt %]	*n* [1/nm^2]	*l* [nm]	*n*(EG) [1/nm^2]
L3-NP	++	5557[b]	−1.4 ± 0.1	30	0.09	45 ± 1	0.56 ± 0.02	2.58 ± 0.07	68 ± 2.8
L2-NP	++	2737[b]	−3.2 ± 0.1	23	0.08	33 ± 1	0.69 ± 0.03	1.83 ± 0.06	39 ± 1.8
L1-NP	−	464				23 ± 1	2.46 ± 0.14	1.27 ± 0.06	7 ± 0.4
D2-NP	++	2477	−9.8 ± 0.1	19	0.10	32 ± 1	0.73 ± 0.03	1.77 ± 0.06	26 ± 1.2
D1-NP	+	789	−32.1 ± 0.1	115 (30)[c]	0.16	23 ± 1	1.45 ± 0.08	1.27 ± 0.06	13 ± 0.7
OA-NP	−	268		20 ($CHCl_3$)	0.24 ($CHCl_3$)	13 ± 1	2.14 ± 0.19	0.92 ± 0.07	

[a] Zeta-potential (ξ) measurements were performed in 0.1 M HEPES buffer solution (pH = 7.4) at 25 °C, indicated as H1. The *z*-average diameter (D_z) and the corresponding polydispersity index (PDI) were determined by dynamic light scattering (DLS) in 0.1 M HEPES buffer solution with physiological NaCl concentration (pH = 7.4, 150 mM NaCl), indicated as H2. Stabilizer mass fraction (*m*(TGA), Figure S6) in wt %, measured from TGA using a value of 3.67 nm for the iron oxide core radius. Stabilizer grafting density *n*, organic dry-shell thickness *l*, and monomer ethylene glycol (EG) surface density *n*(EG) are obtained by assuming an organic shell density ρ of 1.08 and 0.81 g/cm^3 for the ethylene-glycol-based stabilizers and oleylamine, respectively. The errors for *n*, *l*, and *n*(EG) reflect the uncertainty of the TGA measurement. The symbols "++", "+" and "−" represent "good", "moderate", and "no" water solubility, respectively. [b] Most intensive peak in the MALDI-mass spectra. [c] The solvation process of D1-NPs after transfer to water (after predissolution in $CHCl_3$) is a kinetically very slow process. The indicated value D_z of D1-NP is the value that was obtained directly after NP dispersion. The value in brackets was obtained after 77 days equilibration in aqueous solution. The value of the hydrodynamic size (30 nm) for D1-NP indicates that the particles are still not fully dispersed.

TEM analysis (7.3 ± 1.2 nm). The slightly lower value obtained *via* XRD in comparison to TEM analysis is probably due to the presence of less ordered material at the surface of the particles that do not contribute to the XRD signal.[16]

Nanoparticle Stabilization and Purification. Particle stabilization by ligand exchange with hydrophilic, ethylene-glycol-based stabilizers was optimized in terms of solvent type and reaction conditions. The best results, with regard to the subsequent degree of particle dispersion and stability in aqueous media, were found for EtOH as solvent, treatment at 50 °C for 24 h and use of a 4-fold weight excess of the stabilizer compared to the oleylamine-stabilized Fe_3O_4 NPs (details given in the Materials and Methods). From TGA measurements as described below, the highest ratio determined after stabilization between the adsorbed dispersant mass and the iron oxide core mass was 0.8 for L3-NP (corresponding to a molar excess of 5.6 for L3-NP; see Materials and Methods) in comparison to the provided mass ratio of 4.0, demonstrating that we had functionalized the particles with dispersant excess. Using $CHCl_3$ as an alternative solvent, the obtained particles (D2-NP) turned out to have a lower stability toward thermally induced aggregation.

After ligand exchange, the replaced oleylamine was removed from solution by adding hexane to the particle suspension. The hexane-soluble oleylamine remained in solution, whereas the modified particles precipitated and were subsequently collected by a magnet; the oleylamine was then removed by decantation. The presence of oleylamine in the hexane phase was determined by ^{1}H NMR spectroscopy (Supporting Information, Figure S3). After a second precipitation step, the particles were dried and resuspended in water.

Particle purification, especially the removal of excess uncoupled stabilizer molecules, is a key aspect of pure NP sample preparation (see Supporting Information). The presence of uncoupled stabilizers can have a detrimental effect on particle solution stability and, moreover, results in the overestimation of the grafting density (*e.g.*, when calculated from TGA data). Our particles were therefore carefully purified by centrifuge-assisted ultrafiltration (L3-NP, L2-NP, and D2-NP), dialysis (D1-NP), and precipitation (L1-NP). The use of different purification methods was necessary due to different colloidal properties (such as colloidal stability and solubility) of the different particles. However, for the particles L3-, L2-, and D2-NP, a common purification method (ultrafiltration) was applied, which ensures consistency in comparison of the particle properties.

Chemical and Physical Nanoparticle Characterization. Table 1 summarizes the properties of the NPs for the different *M* and architectures of the stabilizers, both oleylamine-capped (OA-NP) and dendritic (D1-NP, D2-NP) or linear PEG (L1-NP, L2-NP, L3-NP) analogues. The TEM image of L3-NP (Figure S2B) demonstrates that the deposited particles are well-separated from each other, showing no signs of agglomeration. Additionally, the mean interparticle distance of L3-NP was found to be considerably larger than the interparticle distance of OA-NP, reflecting the presence of a thicker organic shell for L3-NP. The NP core size distributions of OA-NP and L3-NP were also compared, and it is clear that the ligand exchange did not induce any significant size changes (Figure S2C). Thermogravimetric analysis (TGA) was used to determine the relative amount of organic material (oleylamine and PEG stabilizers, respectively) bound to the NP surface by monitoring the mass loss following thermal oxidation up to 400 °C. Using the average core size extracted from TEM images, the surface grafting density *n* (number of molecules per unit area) was quantitatively estimated. FT-IR spectroscopic measurements further confirmed the successful ligand exchange reaction as implied in Figure 1 (see Supporting Information Figure S4, Figure S5, and Table S1).

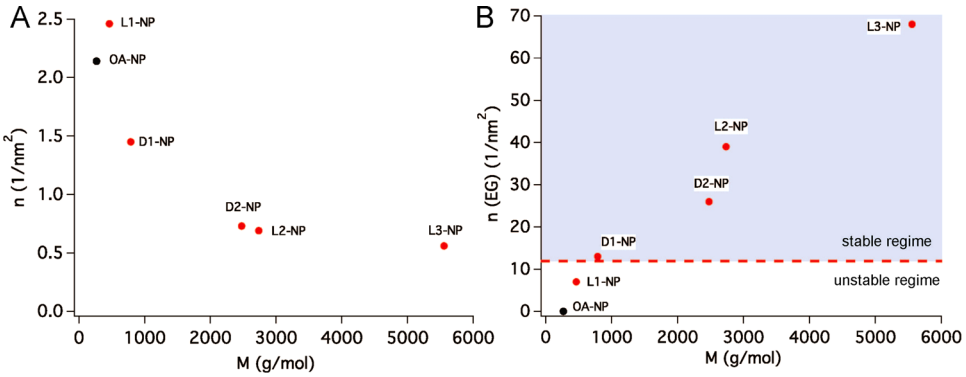

Figure 3. (A) Dispersant molecular grafting density (molecules per nm^2 surface area) *n versus* dispersant molecular weight *M*. (B) Ethylene glycol (EG) monomer surface density *n*(EG) *versus* dispersant molecular weight *M*.

Dispersant Grafting Density and Dry Shell Thickness. A first observation that emerges from the data in Table 1 is a correlation between the dispersant grafting density (*n*) and its molecular weight (*M*), irrespective of the molecular architecture. As Figure 3A demonstrates, decreasing *M* of the stabilizer resulted in higher saturation grafting densities. The lowest molecular grafting density (0.56 nm^{-2}) was measured for the highest-molecular-weight L3, whereas an almost 3-fold increase (1.45 nm^{-2}) was observed for the low-molecular-weight, first-generation dendron D1. This effect can be explained by steric hindrance between the dispersant molecules during adsorption, as previously reported on flat surfaces for similar assembly protocols.[49] The two dispersants L2 and D2 with comparable *M* showed similar molecular grafting densities, 0.69 and 0.73 nm^{-2}, respectively, irrespective of the differences in molecular architecture. The analogy in stabilizer *M* and grafting density makes these two systems ideal candidates to investigate the sole influence of stabilizer architecture on particle properties, in particular, colloidal stability, hydrodynamic radius, and aggregation behavior.

An analogous trend with molecular weight can also be observed for the dry thickness of the polymer adlayer. Higher-molecular-weight PEG leads to thicker dispersant shells. Interestingly, even though D1-NP and L1-NP have the same dry adlayer thickness *l* (*i.e.*, same amount of organic mass adsorbed), L1-NP is not water-soluble, in contrast to D1-NP. We note two differences between the stabilizer characteristics when comparing the two particle types: (i) the dispersant molecular weight of D1 is higher (by 0.3 kDa) and (ii) D1 has the higher percentage of ethylene glycol content relative to L1 (percentage EG content of 61 and 35 wt % relative to the overall *M* for D1 and L1, respectively). Both aspects are likely to contribute to the much improved water solubility of D1-NP and account for the 2× higher EG monomer surface density *n*(EG), which is now above a critical value of *ca.* 12 EG/nm^2, separating the unstable and stable regimes (Figure 3B). Interestingly, in several past studies on flat 2D surfaces, a value of >12−15 monomer units/nm^2 has been found to be key to surface passivation and anti-adhesive ("antifouling") properties of both PEG[49] and poly(methyl oxazoline)-based polymeric assembly systems.[50]

Solubility. All particles except L1-NP and OA-NP were soluble in aqueous solutions after freeze-drying, but among the different systems, different solubility kinetics were observed.

In particular, particles stabilized by dendritic molecules (D2-NP) showed a much faster solubilization in aqueous solution compared to linear PEG analogues. D2-NP became suspended in H_2O at room temperature within seconds, whereas it took ∼1 h for L2-NP and several hours for L3-NP to disperse completely. For D1-NP, the former good aqueous solubility was significantly reduced after the freeze-drying procedure. Interestingly, if after freeze-drying the D1-NP particles were suspended first in $CHCl_3$, which was subsequently evaporated, the air-dried particles could be solubilized in water again. Initial solvation in $CHCl_3$ may help rehydration of the shell, while rehydration of the dry, fully collapsed state was not possible or kinetically very slow. The rate of dispersion was nevertheless slow (several hours), and traces of particles were not soluble at all. These insoluble aggregates were removed from the particle solution *via* centrifugation before further characterization. However, for L3-, L2-, and D2-NP, the "chloroform procedure" was not necessary to obtain fast and efficient solubilization in aqueous solutions.

A similar solubility behavior was observed using $CHCl_3$ as a more hydrophobic but also good solvent for EG-based dispersants. D2-NP and D1-NP were suspended within seconds, for L3-NP and L2-NP, it took several hours until all of the particles were completely suspended. For L1-NP, the dispersion process in $CHCl_3$ took even more time; even after 24 h, not all particles were suspended, and larger, optically visible, gel-like agglomerates were observed. In water, L1-NPs were completely insoluble.

The different solubility behavior between linear and dendritically stabilized NPs is directly linked to the different conformation of the dry dispersant shells. Upon drying, the linear polymer chains of neighboring particles

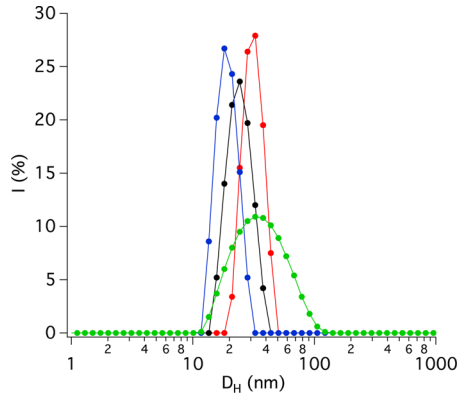

Figure 4. Intensity (*I*)-weighted distribution of the hydrodynamic particle diameter D_H of the stabilized NPs obtained by DLS measurements in H2 buffer at 25 °C after complete solubilization for L3-NP (red), L2-NP (black), D2-NP (blue), and D1-NP (green). The curves for D1-NP are the equilibrium curves, recorded 4 months after dispersion.

are likely to interdigitate, leading to smaller interparticle separations and thus increased van der Waals interactions, resulting in a reduced dispersion rate. Conversely, the dendritic stabilizers form a much more compact shell, as also demonstrated for the dendritic adlayers on flat titanium oxide in our earlier studies.[36]

Hydrodynamic Radius and Colloidal Stability. DLS measurements were performed in order to determine the hydrodynamic diameter of the stabilized NPs in physiological buffer solution (H2 buffer) as listed in Table 1. Figure 4 illustrates the intensity-weighted diameter distributions of the NPs suspended in H2 (the DLS data in pure water and H2 are very similar).

D2-NP had the lowest *z*-average diameter (D_z) (19 nm) followed by L2-NP (23 nm) and L3-NP (30 nm). We note here that the reported D_z for D1-NP does not correspond to the calculated single-particle hydrodynamic diameter since residual agglomeration was present, even after several months in solution (see Figure 5). This corresponds to an estimated hydrated organic shell thickness of approximately 6, 8, and 11 (±1.2) nm for D2-NP, L2-NP, and L3-NP, respectively (iron oxide core diameter = 7.3 nm). However, due to the presence of a hydration layer, DLS result may slightly overestimate the "real" hydrated shell thickness. The values for L2-NP and L3-NP are comparable to the thickness of hydrated PEG brushes on flat 2D surfaces,[36,51,52] and therefore, the particle hydrodynamic diameter data provide strong evidence for the presence of single, non-agglomerated particles.

A point of major interest is the fact that D2-NPs are significantly smaller than L2-NPs, despite both particles containing practically the same amount of organic material (same organic dry-shell thickness) and dispersant grafting density (Table 1). This confirms our previous observations on flat surfaces that dendritic molecules form a thinner, more compact, and less hydrated shell in comparison to linear PEG dispersants.[36]

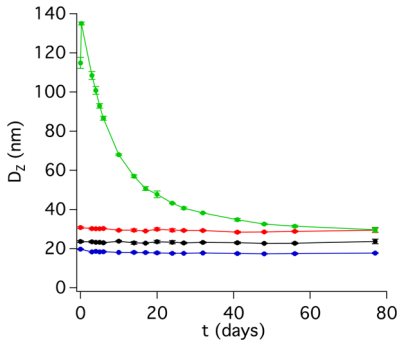

Figure 5. Long-term solution stability test of L3-NP (red), L2-NP (black), D2-NP (blue), and D1-NP (green). The test was performed in the physiological buffer H2 (0.1 M HEPES, pH = 7.4, 150 mM NaCl) at room temperature (22−23 °C) and the *z*-average diameter D_z (nm), obtained by DLS measurements, recorded over time *t* up to 77 days.

The colloidal long-term stability of the particles in aqueous solution was also quantified *via* DLS measurements. In Figure 5, D_z values of L3-NP, L2-NP, D2-NP, and D1-NP suspended in H2 are shown as a function of time.

No change in size or agglomeration was observed for L3-NP, L2-NP, and D2-NP over at least 77 days at room temperature in 0.1 M H2 buffer. However, as discussed in the preceding section on solubilization kinetics, D1-NP showed a constant decrease of D_z after NP solution preparation, from a value of >100 nm (*i.e.*, indicating substantial agglomeration) to an equilibrium size of around 30 nm after 77 days.

The long-term stability test was also performed in pure water solution with a very similar outcome (Figure S7) as well as under physiological salt conditions at 37 °C, colloidal stability being exhibited up to the 31 days of the test (Figure S8).

Zeta-Potential. Zeta-potential measurements performed in 0.1 M HEPES solution at physiological pH = 7.4 (H1 buffer) highlighted that all stabilized particles had a negative surface charge (Table 1). In contrast to the DLS measurements, the zeta-potential measurements were performed in the absence of NaCl because NaCl caused very fast oxidation of the electrodes during the measurements. L3-NP and L2-NP showed very low zeta-potentials of −1.4 and −3.2 mV, whereas for D2-NP and D1-NP, values of −9.8 and −32.1 mV were obtained. These large differences between the linear and dendritic cases clearly reflected the balance between two independent parameters: the hydrated shell thickness and the surface-grafting density, with the latter being especially important for dianionic ligands, such as catechols or phosphonates. The adsorption of the catechol derivate *via* the formation of a chelating bond results in the formation of an additional negative surface charge, due to the dianionic character of the deprotonated catechol group. Amstad *et al.* reported that, upon surface modification of iron oxide NPs with PEG-gallol (a catechol derivate) conjugates, the

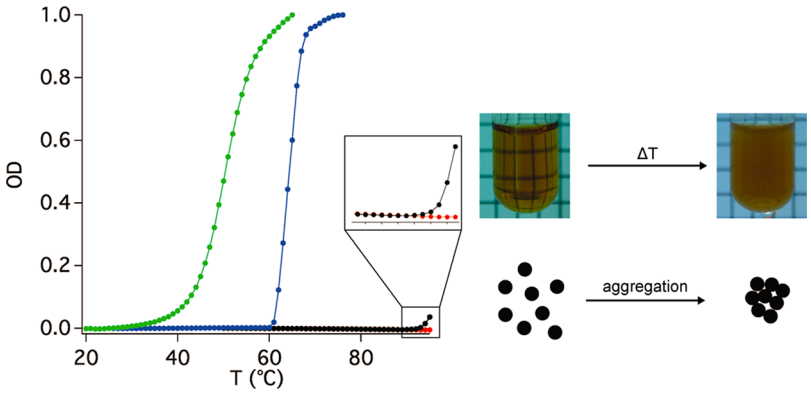

Figure 6. Left: Cloud-point (CP) determination of L3-NP (red), L2-NP (black), D2-NP (blue), and D1-NP (green) in 0.1 M HEPES solution (H2, 150 mM NaCl, pH = 7.4). The optical density (OD; normalized) was recorded *via* UV−vis spectroscopy at a wavelength of 600 nm as a function of the temperature (*T*). Right: Images and cartoon of the clouding process of D2-NP during heating of the sample above the CP temperature.

IEP of the NPs shifted significantly toward more acidic values (IEP = 4.2).[53] Basly *et al.*[30] and Daou *et al.*[43] also investigated the adsorption of EG-based phosphonates onto iron oxide NPs and found a significant increase in the zeta-potential (to more negative values) after immobilization of the phosphonates. The absolute value of surface charge also increased with increasing phosphonate grafting density.[43]

Conversely, it is expected that with increasing hydrated shell thickness the zeta-potential decreases, as a consequence of more efficient shielding of the interfacial surface charge. Therefore, for L3-NP and L2-NP, the surface charge is likely to be shielded more effectively in comparison to the D2-NP and D1-NP. This is confirmed by a slightly more negative zeta-potential for D2-NP compared to L2-NP since, for similar grafting densities, D2-NP has a lower hydrated shell thickness. For D1-NP, both parameters, the low shell thickness and the high grafting density, contribute to the high effective negative surface charge.

For L3-NP and L2-NP, the obtained surface charges are too low to contribute effectively to stabilization based on electrostatic interactions. However, for D1-NP, electrostatic repulsion as a consequence of the high zeta-potential of −32.1 mV might contribute significantly to or even exclusively determine its colloidal solution stability.

Nanoparticle Cloud Points. The thermoresponsive behavior, that is, the determination of the *T*-dependent aggregation (or "cloud point") of the particles in aqueous solutions was investigated *via* UV−vis spectroscopic measurements. Figure 6 shows the temperature-dependent optical density (OD) of the particles L3-NP, L2-NP, D2-NP, and D1-NP in physiological buffer solution H2. The specific cloud-point (CP) temperatures of all free stabilizers and the corresponding stabilized particles in solutions of different ionic strengths are listed in Table 2.

Figure 6 and Table 2 demonstrate that the CP of the dendritic-stabilized NPs are substantially lower than those of the linear-stabilized analogues. In physiological buffer solution (Figure 6), L3-NP does not show clouding below 95 °C, whereas L2-NP starts to cloud at around 90 °C (see inset in Figure 6 left). In contrast, the dendritic analogue of L2-NP, D2-NP, already shows clouding at a temperature of around 60 °C. This observation primarily reflects the comparatively lower CPs of the "free" dendritic molecules in comparison to the linear PEG chains (Table 2).[36,54] Reducing further the stabilizer *M*, D1-NP shows already a slight increase in the OD at temperatures as low as 25 °C with a sharper increase at around 40 °C.

TABLE 2. Compilation of the Cloud-Point Temperatures of the Free Stabilizers and the Stabilized NPs in 0.1 M HEPES buffer (pH = 7.4) in Solutions of Varying NaCl Concentrations (10, 150, 500, and 1000 mM NaCl) Obtained *via* UV−Vis Spectroscopic Measurements (Experimental Error Is Estimated To Be ±1 °C)

	CP temperatures [°C]					
	1000 mM		1000 mM	500 mM	150 mM	10 mM
L3	no CP	L3-NP	82	90	no CP	no CP
L2	no CP	L2-NP	80	87	90−92	no CP
D2	60	D2-NP	45	52	60	72
D1	no CP	D1-NP	not soluble	not soluble	25−40[a]	70−80[a]

[a] The increase of the optical density (OD) takes place in a relative broad temperature range. No sharp CP detectable.

Clouding Reversibility. In order to study the reversibility of the temperature-induced aggregation, the NP solutions were heated from room temperature (25 °C) to above their CP temperature. Subsequently, the solution was cooled again to room temperature with the same rate as for the heating phase (1 °C/min) while aggregation was monitored *via* UV−vis spectroscopy. To ensure a significant degree of clouding for all NPs investigated, the clouding reversibility experiments (Figures 7 and 8) were performed in a solution of increased ionic strength (1000 mM NaCl) instead of using a solution with an ionic strength of biomedical

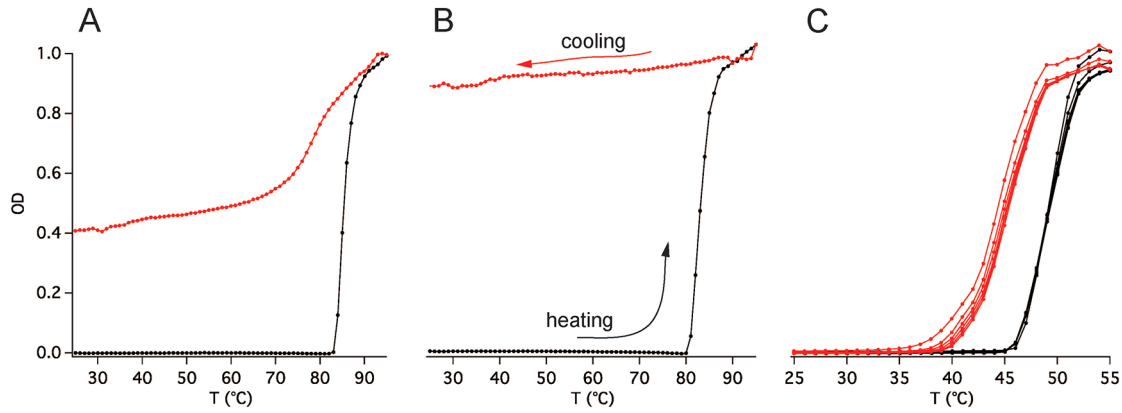

Figure 7. Heating curves (black) and cooling curves (red) of the L3-NP (left, A), L2-NP (middle, B), and D2-NP (right, C) in 0.1 M HEPES buffered solution (1000 mM NaCl), demonstrating (ir)reversibility of the temperature-dependent clouding for the different NPs. The optical density (OD; normalized) was recorded as a function of the temperature *T via* UV−vis spectroscopy at a wavelength of 600 nm. For D2-NP, six heating−cooling cycles were recorded in order to illustrate the reversibility of this system. D1-NP was not soluble under these buffer conditions.

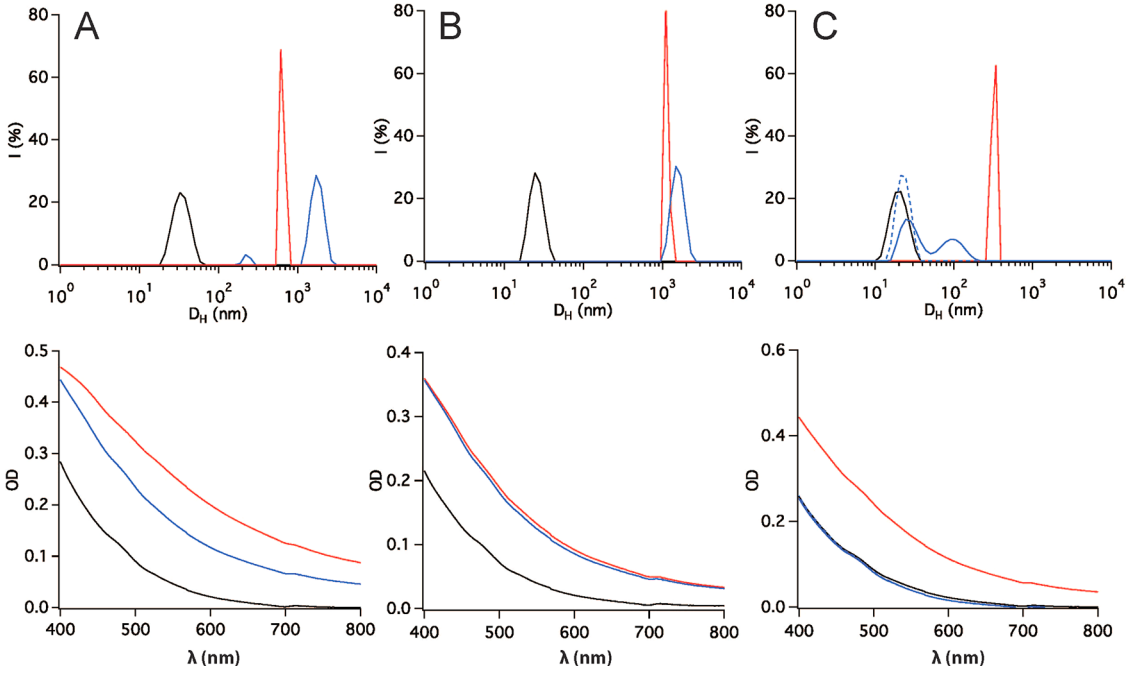

Figure 8. Aggregation reversibility test of L3-NP (A), L2-NP (B), and D2-NP (C) in 0.1 M HEPES solution (1000 mM NaCl). The samples were heated to 90 °C (above the cloud point (CP) of all NPs) for 30 min and cooled to 25 °C again. DLS (top graphs, distribution of the intensity-weighted hydrodynamic particle size D_H and signal intensity *I*) and UV−vis measurements (lower graphs, wavelength λ and optical density OD) were performed *in situ* at 25 °C before heating (black curves), at 90 °C (red curves), and 30 min after cooling to 25 °C (blue curves). The dashed blue lines in C represent the size distribution curves and the UV−vis spectra of D2-NP after the heating experiment and 2 days of equilibration time.

relevance (150 mM NaCl), for which no clouding was observable for L3-NP.

Figure 7 shows the corresponding heating/cooling curves for the different NP suspensions (L3-NP, L2-NP, and D2-NP) in HEPES buffer of high ionic strength (0.1 M HEPES buffer, 1000 mM NaCl). For L3-NP (Figure 7A) and L2-NP (Figure 7B), similar heating curves were obtained with clouding temperatures of 82 and 80 °C, respectively. Upon cooling, the OD of the L3-NP solution decreased but did not reach the initial value observed at 25 °C before the heating cycle. For L2-NP, the OD decreased only marginally. For both samples, the NPs remained in an irreversibly aggregated state even after reaching the initial temperature (25 °C), finally resulting in sedimentation of aggregated particles (Figure S9).

An entirely different behavior was observed for D2-NP (Figure 7C). After heating to 55 °C, the curve returned to the initial OD value when cooled to 25 °C. Furthermore, heating−cooling cycles were performed six times in a row on the same sample without significant changes in the OD curves or particle sedimentation being observed. Clouding of D1-NP turned out

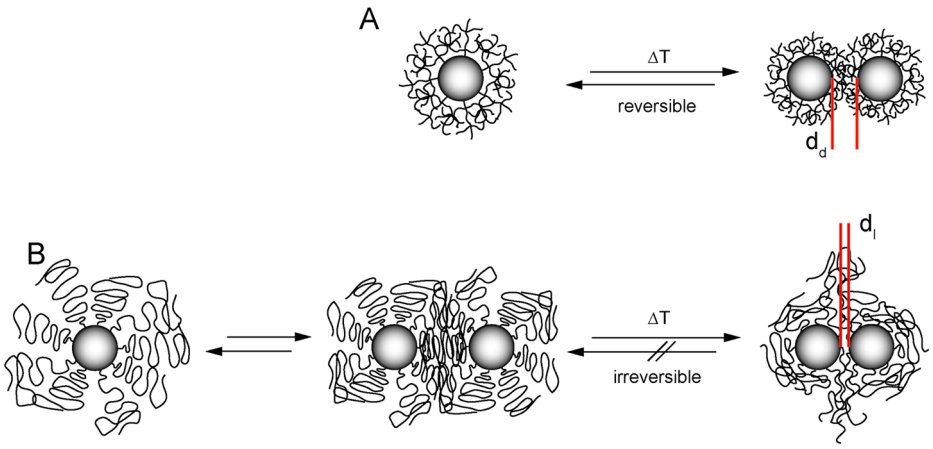

Figure 9. Proposed mechanism of the temperature-induced clouding process. (A) Reversible aggregation of dendron-stabilized particles, d_d = interparticle "minimum distance" for dendritic-stabilized particles. (B) Clouding of linear polymer-stabilized NPs, d_l = interparticle "minimum distance" for linear-stabilized particles. This proposed interpretation is also (qualitatively) supported by thermal collapse data reported for dendronized polymers.[59,60]

to be basically irreversible, similar to L2-NP and L3-NP (data not shown here).

So far, the reported experiments were performed with the upper temperature limit being 10 °C above the relevant particle CP. To investigate whether the great differences in reversibility between the tested NPs could simply reflect differences in the maximum temperature used, a second experiment was performed, in which the same maximum temperatures and the same buffer composition were chosen for all probes. To this end, all samples were rapidly (10 °C/min) heated to 90 °C, maintained at this temperature for 30 min, and cooled to 25 °C (10 °C/min). The experiment was monitored *in situ* with both UV−vis spectroscopy and DLS (Figure 8). Figure 8 demonstrates that all NPs aggregated at T = 90 °C, indicated by the change of the UV−vis spectra and the DLS curves. After cooling, L3-NP and L2-NP particles remained in the aggregated state, according to both UV−vis and DLS results, and finally sedimented, as observed in the first test series with different maximum temperatures. In stark contrast to the linear polymer constructs, complete declouding was observed for D2-NP upon returning to room temperature, with very similar UV−vis spectra being measured before and after the heating process. Again, no particle sedimentation was observed for D2-NP, although the particles returned to a much less agglomerated state (D_z = 37 nm) immediately after cooling, rather than to the original value of D_z = 19 nm that was measured before the heating cycle. However, after several days of equilibration at room temperature, the hydrodynamic size of the particles further decreased to 22 nm, a value close to the value measured before the heating experiment.

Discussion. In summary, these experiments demonstrate that the physical properties of NPs stabilized by hydrophilic dispersants with linear and dendritic architecture are different, particularly with regard to surface charge, solubility, and degree of reversibility of thermally induced aggregation in aqueous solutions. The difference is especially remarkable between the L2-NP and D2-NP samples, for which the relative amounts of organic material on the iron oxide NPs are essentially the same. Also when compared to L3-NP, D2-NP dispersions were much more stable even though the relative organic mass adsorbed on the iron oxide core was 29% lower for D2-NP compared to L3-NP. This underlines the essential role played by the molecular interface architecture, which for our polymer−particle system has a more significant influence on the particle aggregation stability than the M of the stabilizer or the absolute amount of adsorbed organic material.

The advantageous effect of the dendritic architecture on the reversibility of aggregation is most likely a consequence of differences in the chain dynamics and viscoelastic properties of the adlayer compared to the linear analogue. As reported in the literature, dendrimers, especially of higher generations, have a very crowded and densely packed surface at their periphery. They exhibit a lower hydrodynamic radius and a lower intrinsic viscosity compared to linear polymers with the same M, indicating a higher degree of packing.[55,56]

Specifically, we have demonstrated in an earlier publication (using optical and quartz crystal microbalance sensing) that OEG dendrons form a much stiffer and much less hydrated surface film on 2D flat titanium oxide surfaces compared to linear PEG polymer brushes with a similar M and comparable dry adsorbed mass.[36] We therefore propose that the observed differences in the reversibility of the dendron and linear chain surfaces are likely due to the mechanisms schematically depicted in Figure 9. Two NPs separated by a dense, stiff dendron shell (Figure 9A) are more reminiscent of a hard−hard contact with a limited contact area and reduced adhesion, in comparison to the much softer, more hydrated linear polymer shell for which entanglement of chains from neighboring particles is more likely

to happen, resulting in irreversible kinetic trapping during the clouding process. The stiff dendron architecture is furthermore expected to be more efficient in preventing two iron oxide cores from approaching a critical lower separation distance, at which irreversible aggregation (due to strong van der Waals interactions) and subsequent sedimentation is induced. Conversely, a different scenario is proposed for particles stabilized by linear PEG, as shown in Figure 9B. In the early stage of clouding, the polymer chains of different particles can penetrate each other, resulting in loosely connected agglomerates. This first clouding step might still be reversible. However, in the next step, the flexible linear polymer chains can be squeezed out of the volume between the two approaching particles, resulting in such small interparticle distances that reversibility of interparticle interaction is compromised, resulting in larger aggregates and finally sedimentation. Interestingly, in an earlier mechanistic study, the same type of dendritic OEG structures in dendronized polymers were found to result in much sharper and nearly hysteresis-free transitions,[54,57] in contrast to polymer analogues with linear OEG side chains that showed pronounced hysteresis.[58] Although structurally different than the system studied in this work, the combined experimental data suggest a common molecular mechanism accounting for the differences in thermal collapse/agglomeration and aggregation behavior, likely based on an initial dehydration of the outermost generation layer as temperature is increased, followed by dehydration of the inner parts of the dendron.[59,60] Such a mechanism could account for a pronounced resistance of dendritic structures to interdigitation of chains, thus favoring clouding reversibility and low levels of hysteresis.

CONCLUSIONS

This work highlights the great importance of interfacial polymer architecture for the interaction between sterically stabilized NPs and the reversibility/irreversibility of agglomeration and finally aggregation—a key issue for many applications using NPs, which range from particle-reinforced materials to targeted *in vitro* and *in vivo* diagnostics. The excellent colloidal stability of the dendron-stabilized NPs, the reversibility of temperature-induced aggregation, as well as a relatively low overall hydrodynamic size of the nanoparticles, make this type of macromolecule an attractive, well-controlled surface modifier and an alternative to the conventional linear brush systems, particularly for bio-oriented applications. In combination with the efficient presentation of terminally bound (bio)ligands at high surface density, we expect this platform to have superior performance, especially for targeting applications where multivalent interactions are key for affinity or avidity, potentially justifying the higher costs associated with the synthesis of monodisperse dendrons. Furthermore, the results of this study confirm the great potential of nitro-catechols as a single-foot, essentially irreversibly binding anchor for iron oxides, not suffering from the undesirable oxidation and reversibility of attachment observed for "conventional", unsubstituted catechol anchors (DOPA, Dopamine).[61−63]

A second advantage of dendron-stabilized NPs compared to linear brushes relates to the observation of a substantially reduced shell thickness to achieve the same degree of dispersion stability. This is potentially of great value for applications where limiting the NP size to the tens of nanometers range is key, for example, in cellular uptake[33,34] and biomedical applications that involve the crossing of tissue barriers—a crucial factor in the exploitation of the EPR (enhanced permeation effect) for cancer therapy and diagnostics.[32,35]

Finally, the observation of very different physicochemical properties of the dendron compared to the linear PEG (low *versus* high hydration, stiffer *versus* softer shell, thinner *versus* thicker film) poses a number of fundamental questions about the mechanistic aspects of stability and aggregation reversibility for NPs and the antifouling properties as observed on flat surfaces,[36] usually discussed solely in the context of steric repulsion, excluded volume effects, and hydration.[64,65] Theoretical studies may be able to dissect the underlying mechanisms and resulting differences between the linear and dendritic surface modifiers in matters of NP stability and antifouling behavior.

MATERIALS AND METHODS

Materials. DMF (puriss, absolute, 99.8% (GC), over molecular sieve, $H_2O \leq 0.01\%$) was purchased from Sigma Aldrich (Buchs, Switzerland). Nitrogen ($\geq 99.999\%$) was obtained from PanGas (Dagmarsellen, Switzerland). 4-(2-Hydroxyethyl)piperazine-1-ethanesulfonic acid (HEPES) was obtained from Fluka Chemical (Buchs, Switzerland). Iron(III) acetylacetonate ($Fe(acac)_3$, $\geq 99.9\%$) and oleylamine (70%) were obtained from Aldrich Fine Chemicals (Buchs, Switzerland). All water used for surface experiments and buffer solutions was prepared by a Millipore water purification system (Milli-Q system; Millipore, 18.2 Ω, TOC ≤ 5 ppb). All buffers were prepared with Milli-Q water, stored in the refrigerator at 4 °C, and filtered (0.2 μm) before use. PEG-2300 Da-NHS (methoxy poly(ethylene glycol) carboxy methyl ester, L2(NHS), M = 2300 Da) and PEG-5000 Da-NHS (methoxy poly(ethylene glycol) carboxy methyl ester, L3(NHS), M = 5000 Da) were purchased from JenKem Technology (USA). The synthesis of the surface modifiers (L1, L2, L3, D1, and D2), and the NMR spectra of the compounds can be found in the Supporting Information. Other reagents and solvents were purchased at reagent grade and used without further purification. Silica gel 60 (230−400 mesh, Fluka Chemical) was used as a stationary phase for column chromatography. Thin-layer chromatography plates (silica gel 60 with fluorescent indicator UV_{254} coated on 0.20 mm aluminum sheets) were purchased from Macherey-Nagel (Düren, Germany). Preparative thin-layer chromatography (TLC) plates (silica gel 60 with fluorescent indicator UV_{254} coated on glass plates 0.20 mm, 20 × 20 cm^2) were purchased from Merck KGaA (Darmstadt, Germany).

Chemical and Physical Characterization. ^1H and ^{13}C NMR spectroscopic measurements were recorded on Bruker Avance 300 and

500 spectrometers (^{13}C NMR frequencies of 75.5 and 126, respectively) at room temperature. The signal from the specific solvent was used as an internal standard for the determination of the chemical shift ($CDCl_3$, ^1H: 7.26 ppm, ^{13}C: 77.36 ppm; CD_2Cl_2, ^1H: 5.33 ppm, ^{13}C: 54.24 ppm; methanol-d_4, ^1H: 3.34 ppm, ^{13}C: 49.86 ppm).

Mass spectrometry (MS) measurements were performed by the MS-service of the Laboratory for Organic Chemistry at ETH Zürich (MALDI-TOF: Bruker UltraFlex II, MALDI-FTICR-MS: IonSpec (Varian) Ultima, HiResESI: Bruker Daltonics maxis, UHR-TOF).

Elemental analysis measurements were performed by the Micro-Laboratory of the Laboratory for Organic Chemistry at ETH Zurich.

The infrared spectra were recorded on a Bruker IFS 66v FT-IR spectrometer (DTGS detector) in transmission mode as a KBr pellet in the spectral range from 400 to 4000 cm^{-1} at a resolution of 1 cm^{-1} and 64 scans. A vacuum of <2 mbar was applied during the measurement to avoid interfering signals mainly originating from H_2O and CO_2.

Transmission Electron Microscopy (TEM). TEM was used to evaluate the core-size distribution, morphology, and crystallinity of the iron oxide NPs. The measurements were performed on a Philips CM12 microscope (100 kV) equipped with a LaB_6 filament as an electron source. For high-resolution TEM (HRTEM) measurements, a Tecnai F30 (FEI, 300 kV) was used, which was equipped with a Schottky field-emission gun (FEG).

A drop (4 μL, 1 mg/mL in H_2O) of the NP stock solution was placed on a carbon-coated Cu grid (300 mesh) with holes in the carbon support (diameter of the holes 3.5 μm). The drop was allowed to dry on the grid for at least 1 h. Then, 8−10 pictures with in total 5499 particles were used to evaluate the particle size distribution. For the image analysis, a custom-written algorithm located the center of each particle, calculated the particle area, and extracted the radius assuming a spherical shape. A bin size of 0.05 nm was chosen for the creation of the particle size histogram.

X-ray Diffraction (XRD). XRD measurements were used to evaluate the crystal structure of the nanocrsystals, the size of crystalline domains, and the purity of the crystal phase. The measurements were performed on a Philips PW 1800 instrument in the reflection mode using a Cu Kα radiation (λ = 0.15410 nm), equipped with a post-sample monochromator. Then, 0.5 mL (10 mg/mL dissolved in hexane) of the oleylamine-stabilized particle solution was allowed to dry onto a sapphire substrate. The measurement was performed between the angles of 20 and 90°. To calculate the mean size of the crystalline domains, the Scherrer equation was applied ($D = (K \times \lambda)/\beta \times \cos \Theta$); D = mean size of the crystalline domain, λ = X-ray wavelength, K = shape factor, β = full width at half-maximum (fwhm) in radians, Θ = Bragg angle. The line width of the (311) plane refraction peak and a shape factor $K = 0.89$ were used for the calculations.[16,66]

Dynamic Light Scattering (DLS) and Zeta-Potential. DLS and zeta-potential measurements were performed using the Zetasizer NS Instrument (Malvern, UK). DLS measurements were performed in the backscattering mode (scattering angle of 173°) at a temperature of 25 °C. Every measurement was performed in a plastic UV−vis cuvette (Plastibrand, Brand GmbH, Wertheim, Germany) and repeated three times on the same sample at a concentration range of 20−100 μg/mL. In this range, the DLS results were independent from the concentration. Nevertheless, in a standard experiment, 50 μL of the NP stock solution was diluted in 1 mL of water or aqueous 0.1 M HEPES buffer solution with varying NaCl concentration (0−1000 mM NaCl). For DLS experiments that were performed at higher temperatures than 25 °C, a glass cuvette was used instead of a plastic cuvette. Zeta-potential measurements were performed at 25 °C in 0.1 M HEPES buffer at physiological pH = 7.4 at the same concentration as for the DLS measurements (50 μg/mL). The obtained values obtained are the average of 10 individual measurements.

Thermogravimetric Analysis (TGA). Thermogravimetric analysis (TGA) was performed with a TGA Q500 V5.3 Build 171 with a heating rate of 10 °C/min in a high-resolution mode (reduction of the heating rate during high mass changes). Next, 1.5−3 mg of the substance was heated from 30 to 600 °C under airflow. The mass loss was recorded as dependent on the temperature. To determine the amount of adsorbed organic mass m(TGA) [wt %] relative to the total particle mass, the mass loss between 150 and 450 °C was used for evaluation.

The mass loss of the organic material that was obtained by TGA and the NP core size obtained by TEM were used to calculate the molecular density n [1/nm^2] of the stabilizer on the NP surface. This value was further used to calculate the EG surface density n(EG) [1/nm^2]. For this, spherical particles with a uniform size distribution (diameter d = 7.3 nm) were assumed and a Fe_3O_4 density[67] of 5.2 g/cm^3 was taken into account. Additionally, for calculation of the adlayer thickness of the organic shell l [nm], homogeneous densities of the organic shell for the ethylene-glycol-based and oleylamine-stabilized particles were assumed to be 1.08 and 0.81 g/cm^3, respectively.[68,69] Due to the similarity of the XRD pattern of magnetite and maghemite NPs, a maximum absolute error of 6% in grafting density is possible, assuming either pure magnetite (5.2 g/cm^3) or pure maghemite[67] (4.9 g/cm^3) as NP core material. However, this error would not change the relative grafting densities since the same particle batch was used for all investigated particles.

Nanoparticle Stabilization and Purification. Fe_3O_4 NPs were synthesized according to literature procedure [46] (see Supporting Information for details). Further stabilization of the iron oxide NPs was performed *via* ligand exchange reaction within the first 12 h after the NP synthesis. The stabilizers (ratio m(stabilizer)/m(Fe_3O_4) = 4:1; 123.4 mg [L3], 133 mg [L2], 100 mg [D2, D1, and L1]) were dissolved/suspended in 15 mL of EtOH in a 100 mL flask (see Table 1 for NP coding). (For L3 and L2, the ratio was slightly higher than 4:1 with respect to the presence of the small fraction of surface-unreactive L3(OH) and L2(OH).) Assuming a monodisperse size of the Fe_3O_4 NP cores, this 4-fold weight excess corresponds a molar excess (number of available molecules per nm^2 divided by the maximum grafting density) of 5.62 (L3-NP), 9.33 (L2-NP), 9.77 (D2-NP), 15.39 (D1-NP), and 15.39 (L1-NP) with regard to the particular maximum grafting density of the stabilized particles. The stabilizer solution was heated to 50 °C, and 2.44 mL (25 mg, 10.24 mg/mL, in hexane) of the NP solution was added. The yellowish stabilizer solution turned black upon addition of the NP solution. The flask was closed, and the reaction mixture was magnetically stirred at a temperature of 50 °C (oil bath temperature) for 24 h. Afterward, 60 mL of hexane was added under continuous stirring to remove the oleylamine that was released from the NP surface upon the ligand exchange process. The NPs precipitated and were collected at the flask sidewall using magnets (N50, 1.40−1.46 T, nickel-plated). After complete NP collection, the clear supernatant was removed and the NPs were washed with 10 mL of hexane, redispersed in 5 mL of $CHCl_3$, and precipitated again in hexane. After removal of the hexane, the particles were left to dry at room temperature for 30 min. Afterward, the particles were redispersed in 20 mL of Milli-Q water (except L1-NP). L3-NP, L2-NP, and D2-NP were purified by ultrafiltration (Amicon Ultra 15 ultrafiltration tubes, Millipore, 50 kDa, 15 mL of H_2O, 3000 rpm, 40 min, five times). D1-NP was purified by dialysis (Spectra/Por dialysis tubes, RC, 25 kDa). L1-NP was purified by precipitation. L1-NP was redispersed in EtOH (3 mL) and precipitation by adding 50 mL of H_2O followed by centrifugation (3000 rpm, 15 min). The decantant was removed, and the particles were redispersed in 3 mL of EtOH. This procedure was repeated five times. After the purification step, the particles were dissolved in 10 mL of H_2O, filtered through a 0.2 μm filter, and lyophilized. L1-NP was lyophilized without filtration. After freeze-drying, we obtained 40.0 (100%, 3.40×10^{-5} mmol), 32.2 (99%, 3.34×10^{-5} mmol), 32.6 (100%, 3.42×10^{-5} mmol), and 27.0 mg (96%, 3.21×10^{-5} mmol) of L3-NP, L2-NP, D2-NP, and D1-NP, respectively, as black-brownish fluffy materials. L1-NP was obtained in a yield of 15 mg (53%, 1.78×10^{-5} mmol) as a black solid substance. For further experiments and measurements, aqueous NP stock solutions of 0.001 mM NP (~1 mg/mL NP in H_2O) were prepared.

Stability Test. The long-term solution stability of the modified particles was quantified using DLS measurements. For the experiments, 50 μL of the NP stock solution was added to 1 mL of pure H_2O and 0.1 M HEPES buffer solution with 150 mM

NaCl at pH = 7.4. The colloidal solution stability of the modified particles was quantified by monitoring D_z (DLS) over time. The measurements were performed at room temperature (22−23 °C) and at 37 °C to mimic elevated body temperature (ThermStat plus, equipped with CombiBox, Vaudaux-Eppendorf, Switzerland). The values obtained are the average of measurements on two independent samples (three measurements per sample).

Cloud-Point Experiments. CPs of the free stabilizers and the modified NPs were mainly determined by using UV−vis spectroscopic measurements. The measurements were performed on a Cary 1E spectrometer (Varian, USA) in UV-transparent quartz glass cuvettes. The optical density (OD, absorbance) of the stabilizer and NP suspensions was recorded during heating of the suspensions from 20 °C up to 95 °C (end temperature varied upon the specific NP system). The CP temperature (T_C) was defined as the temperature where a sharp increase of the absorbance relative to the baseline was observed. The T_C of the stabilizers (L3, L2, D2, and D1) was determined at a polymer/dendron concentration of 0.1 mg/mL. Due to significant absorbance of the nonagglomerated particles at wavelengths <600 nm, the cloud-point experiments were performed at a wavelength of 600 nm. At this wavelength, the optical density was recorded with a heating rate of 1 °C/min. For the determination of the CPs of the stabilized particles, 50 μL of the stock solution was diluted in 1 mL of aqueous HEPES buffer solution (0.1 M HEPES, pH = 7.4) with different NaCl concentrations (0−1000 mM NaCl).

Conflict of Interest: The authors declare no competing financial interest.

Acknowledgment. We thank R. Konradi, E. Rakhmatullina, E.M. Benetti, and E. Reimhult for valuable discussions, and W. Li and A. Zhang for the chemical synthesis of the dendritic precursors D1(PFP) and D2(PFP). We are also grateful to E. Amstad for performing the TEM measurements and helpful discussions. Financial support by the Swiss National Science Foundation (Scientific & Technological Cooperation Program Switzerland−Russia), the NCCR Nanosciences Basel, BASF Switzerland, and MC-IEF-2009-252926 is greatly acknowledged.

Supporting Information Available: Size distribution and TEM images of the OA- and L3-NPs. TGA sensorgram, colloidal stability test, and synthesis of the NPs, and the poly(ethylene glycol)-based surface modifiers. FTIR, ^{1}H, and ^{13}C NMR and mass spectra. This material is available free of charge *via* the Internet at http://pubs.acs.org.

REFERENCES AND NOTES

1. Laurent, S.; Forge, D.; Port, M.; Roch, A.; Robic, C.; Vander Elst, L.; Muller, R. N. Magnetic Iron Oxide Nanoparticles: Synthesis, Stabilization, Vectorization, Physicochemical Characterizations, and Biological Applications. *Chem. Rev.* **2008**, *108*, 2064–2110.
2. Gao, J.; Gu, H.; Xu, B. Multifunctional Magnetic Nanoparticles: Design, Synthesis, and Biomedical Applications. *Acc. Chem. Res.* **2009**, *42*, 1097–1107.
3. Neuberger, T.; Schöpf, B.; Hofmann, H.; Hofmann, M.; von Rechenberg, B. Superparamagnetic Nanoparticles for Biomedical Applications: Possibilities and Limitations of a New Drug Delivery System. *J. Magn. Magn. Mater.* **2005**, *293*, 483–496.
4. Laurent, S.; Dutz, S.; Häfeli, U. O.; Mahmoudi, M. Magnetic Fluid Hyperthermia: Focus on Superparamagnetic Iron Oxide Nanoparticles. *Adv. Colloid Interface Sci.* **2011**, *166*, 8–23.
5. Weissleder, R.; Stark, D. D.; Engelstad, B. L.; Bacon, B. R.; Compton, C. C.; White, D. L.; Jacobs, P.; Lewis, J. Superparamagnetic Iron Oxide—Pharmacokinetics and Toxicity. *Am. J. Roentgenol.* **1989**, *152*, 167–173.
6. Wang, Y.-X.; Hussain, S.; Krestin, G. Superparamagnetic Iron Oxide Contrast Agents: Physicochemical Characteristics and Applications in MRI Imaging. *Eur. Radiol.* **2001**, *11*, 2319–2331.
7. Li, Z.; Wei, L.; Gao, M. Y.; Lei, H. One-Pot Reaction To Synthesize Biocompatible Magnetite Nanoparticles. *Adv. Mater.* **2005**, *17*, 1001–1005.
8. Lutz, J.-F.; Stiller, S.; Hoth, A.; Kaufner, L.; Pison, U.; Cartier, R. One-Pot Synthesis of PEGylated Ultrasmall Iron-Oxide Nanoparticles and Their *In Vivo* Evaluation as Magnetic Resonance Imaging Contrast Agents. *Biomacromolecules* **2006**, *7*, 3132–3138.
9. Amstad, E.; Textor, M.; Reimhult, E. Stabilization and Functionalization of Iron Oxide Nanoparticles for Biomedical Applications. *Nanoscale* **2011**, *3*, 2819–2843.
10. Hu, F. Q.; Wei, L.; Zhou, Z.; Ran, Y. L.; Li, Z.; Gao, M. Y. Preparation of Biocompatible Magnetite Nanocrystals for *In Vivo* Magnetic Resonance Detection of Cancer. *Adv. Mater.* **2006**, *18*, 2553–2556.
11. Sun, C.; Sze, R.; Zhang, M. Folic Acid-PEG Conjugated Superparamagnetic Nanoparticles for Targeted Cellular Uptake and Detection by MRI. *J. Biomed. Mater. Res., Part A* **2006**, *78A*, 550–557.
12. Sun, C.; Du, K.; Fang, C.; Bhattarai, N.; Veiseh, O.; Kievit, F.; Stephen, Z.; Lee, D.; Ellenbogen, R. G.; Ratner, B.; *et al.* PEG-Mediated Synthesis of Highly Dispersive Multifunctional Superparamagnetic Nanoparticles: Their Physicochemical Properties and Function *in Vivo*. *ACS Nano* **2010**, *4*, 2402–2410.
13. Zhang, Y.; Kohler, N.; Zhang, M. Surface Modification of Superparamagnetic Magnetite Nanoparticles and Their Intracellular Uptake. *Biomaterials* **2002**, *23*, 1553–1561.
14. Nitin, N.; LaConte, L. E. W.; Zurkiya, O.; Hu, X.; Bao, G. Functionalization and Peptide-Based Delivery of Magnetic Nanoparticles as an Intracellular MRI Contrast Agent. *J. Biol. Inorg. Chem.* **2004**, *9*, 706–712.
15. Amstad, E.; Gillich, T.; Bilecka, I.; Textor, M.; Reimhult, E. Ultrastable Iron Oxide Nanoparticle Colloidal Suspensions Using Dispersants with Catechol-Derived Anchor Groups. *Nano Lett.* **2009**, *9*, 4042–4048.
16. Sun, J.; Zhou, S.; Hou, P.; Yang, Y.; Weng, J.; Li, X.; Li, M. Synthesis and Characterization of Biocompatible Fe_3O_4 Nanoparticles. *J. Biomed. Mater. Res., Part A* **2007**, *80A*, 333–341.
17. Gupta, A. K.; Curtis, A. S. G. Surface Modified Superparamagnetic Nanoparticles for Drug Delivery: Interaction Studies with Human Fibroblasts in Culture. *J. Mater. Sci.: Mater. Med.* **2004**, *15*, 493–496.
18. Simberg, D.; Duza, T.; Park, J. H.; Essler, M.; Pilch, J.; Zhang, L.; Derfus, A. M.; Yang, M.; Hoffman, R. M.; Bhatia, S.; *et al.* Biomimetic Amplification of Nanoparticle Homing to Tumors. *Proc. Natl. Acad. Sci. U.S.A.* **2007**, *104*, 932–936.
19. Zhu, R.; Jiang, W.; Pu, Y.; Luo, K.; Wu, Y.; He, B.; Gu, Z. Functionalization of Magnetic Nanoparticles with Peptide Dendrimers. *J. Mater. Chem.* **2011**, *21*, 5464–5474.
20. Guo, W.; Li, J. J.; Wang, Y. A.; Peng, X. Luminescent CdSe/CdS Core/Shell Nanocrystals in Dendron Boxes: Superior Chemical, Photochemical and Thermal Stability. *J. Am. Chem. Soc.* **2003**, *125*, 3901–3909.
21. Advincula, R. C. Hybrid Organic−Inorganic Nanomaterials Based on Polythiophene Dendronized Nanoparticles. *Dalton Trans.* **2006**, 2778–2784.
22. Cho, T. J.; Zangmeister, R. A.; MacCuspie, R. I.; Patri, A. K.; Hackley, V. A. Newkome-Type Dendron-Stabilized Gold Nanoparticles: Synthesis, Reactivity, and Stability. *Chem. Mater.* **2011**, *23*, 2665–2676.
23. Grayson, S. M.; Fréchet, J. M. J. Convergent Dendrons and Dendrimers: From Synthesis to Applications. *Chem. Rev.* **2001**, *101*, 3819–3868.
24. Satija, J.; Sai, V. V. R.; Mukherji, S. Dendrimers in Biosensors: Concept and Applications. *J. Mater. Chem.* **2011**, *21*, 14367–14386.
25. Gao, F.; Pan, B.-F.; Zheng, W.-M.; Ao, L.-M.; Gu, H.-C. Study of Streptavidin Coated onto PAMAM Dendrimer Modified Magnetite Nanoparticles. *J. Magn. Magn. Mater.* **2005**, *293*, 48–54.
26. Uzun, K.; Çevik, E.; Şenel, M.; Sözeri, H.; Baykal, A.; Abasyank, M.; Toprak, M. Covalent Immobilization of Invertase on PAMAM-Dendrimer Modified Superparamagnetic Iron Oxide Nanoparticles. *J. Nanopart. Res.* **2010**, *12*, 3057–3067.
27. Svenson, S. Dendrimers as Versatile Platform in Drug Delivery Applications. *Eur. J. Pharm. Biopharm.* **2009**, *71*, 445–462.

28. Liu, M.; Fréchet, J. M. J. Designing Dendrimers for Drug Delivery. *Pharm. Sci. Technol. Today* **1999**, *2*, 393–401.
29. Tomalia, D. A.; Reyna, L. A.; Svenson, S. Dendrimers as Multi-Purpose Nanodevices for Oncology Drug Delivery and Diagnostic Imaging. *Biochem. Soc. Trans.* **2007**, *35*, 61–67.
30. Basly, B.; Felder-Flesch, D.; Perriat, P.; Pourroy, G.; Bégin-Colin, S. Properties and Suspension Stability of Dendronized Iron Oxide Nanoparticles for MRI Applications. *Contrast Media Mol. Imaging* **2011**, *6*, 132–138.
31. Tomlinson, E. Theory and Practice of Site-Specific Drug Delivery. *Adv. Drug Delivery Rev.* **1987**, *1*, 87–198.
32. Cabral, H.; Matsumoto, Y.; Mizuno, K.; Chen, Q.; Murakami, M.; Kimura, M.; Terada, Y.; Kano, M. R.; Miyazono, K.; Uesaka, M.; *et al.* Accumulation of Sub-100 nm Polymeric Micelles in Poorly Permeable Tumours Depends on Size. *Nat. Nanotechnol.* **2011**, *6*, 815–823.
33. Verma, A.; Stellacci, F. Effect of Surface Properties on Nanoparticle−Cell Interactions. *Small* **2010**, *6*, 12–21.
34. Verma, A.; Uzun, O.; Hu, Y.; Hu, Y.; Han, H.-S.; Watson, N.; Chen, S.; Irvine, D. J.; Stellacci, F. Surface-Structure-Regulated Cell-Membrane Penetration by Monolayer-Protected Nanoparticles. *Nat. Mater.* **2008**, *7*, 588–595.
35. Bae, K.; Chung, H.; Park, T. Nanomaterials for Cancer Therapy and Imaging. *Mol. Cells* **2011**, *31*, 295–302.
36. Gillich, T.; Benetti, E. M.; Rakhmatullina, E.; Konradi, R.; Li, W.; Zhang, A.; Schlüter, A. D.; Textor, M. Self-Assembly of Focal Point Oligo-catechol Ethylene Glycol Dendrons on Titanium Oxide Surfaces: Adsorption Kinetics, Surface Characterization, and Nonfouling Properties. *J. Am. Chem. Soc.* **2011**, *133*, 10940–10950.
37. Wang, R.; Yang, J.; Zheng, Z.; Carducci, M. D.; Jiao, J.; Seraphin, S. Dendron-Controlled Nucleation and Growth of Gold Nanoparticles. *Angew. Chem., Int. Ed.* **2001**, *40*, 549–552.
38. Wu, L.; Li, B.-L.; Huang, Y.-Y.; Zhou, H.-F.; He, Y.-M.; Fan, Q.-H. Phosphine Dendrimer-Stabilized Palladium Nanoparticles, a Highly Active and Recyclable Catalyst for the Suzuki−Miyaura Reaction and Hydrogenation. *Org. Lett.* **2006**, *8*, 3605–3608.
39. Love, C. S.; Chechik, V.; Smith, D. K.; Brennan, C. Dendron-Stabilised Gold Nanoparticles: Generation Dependence of Core Size and Thermal Stability. *J. Mater. Chem.* **2004**, *14*, 919–923.
40. Kim, M.-K.; Jeon, Y.-M.; Jeon, W. S.; Kim, H.-J.; Kim, K.; Hong, S. G.; Park, C. G. Novel Dendron-Stabilized Gold Nanoparticles with High Stability and Narrow Size Distribution. *Chem. Commun.* **2001**, 667–668.
41. Pan, B.; Cui, D.; Sheng, Y.; Ozkan, C.; Gao, F.; He, R.; Li, Q.; Xu, P.; Huang, T. Dendrimer-Modified Magnetic Nanoparticles Enhance Efficiency of Gene Delivery System. *Cancer Res.* **2007**, *67*, 8156–8163.
42. Shi, X.; Wang, S. H.; Swanson, S. D.; Ge, S.; Cao, Z.; Van Antwerp, M. E.; Landmark, K. J.; Baker, J. R. Dendrimer-Functionalized Shell-Crosslinked Iron Oxide Nanoparticles for *In-Vivo* Magnetic Resonance Imaging of Tumors. *Adv. Mater.* **2008**, *20*, 1671–1678.
43. Daou, T. J.; Pourroy, G.; Greneche, J. M.; Bertin, A.; Felder-Flesch, D.; Begin-Colin, S. Water Soluble Dendronized Iron Oxide Nanoparticles. *Dalton Trans.* **2009**, 4442–4449.
44. Basly, B.; Felder-Flesch, D.; Perriat, P.; Billotey, C.; Taleb, J.; Pourroy, G.; Begin-Colin, S. Dendronized Iron Oxide Nanoparticles as Contrast Agents for MRI. *Chem. Commun.* **2010**, *46*, 985–987.
45. Amstad, E.; Kohlbrecher, J.; Müller, E.; Schweizer, T.; Textor, M.; Reimhult, E. Triggered Release from Liposomes through Magnetic Actuation of Iron Oxide Nanoparticle Containing Membranes. *Nano Lett.* **2011**, *11*, 1664–1670.
46. Xu, Z.; Shen, C.; Hou, Y.; Gao, H.; Sun, S. Oleylamine as Both Reducing Agent and Stabilizer in a Facile Synthesis of Magnetite Nanoparticles. *Chem. Mater.* **2009**, *21*, 1778–1780.
47. Daou, T. J.; Pourroy, G.; Begin-Colin, S.; Greneche, J. M.; Ulhaq-Bouillet, C.; Legare, P.; Bernhardt, P.; Leuvrey, C.; Rogez, G. Hydrothermal Synthesis of Monodisperse Magnetite Nanoparticles. *Chem. Mater.* **2006**, *18*, 4399–4404.
48. Itoh, H.; Sugimoto, T. Systematic Control of Size, Shape, Structure, and Magnetic Properties of Uniform Magnetite and Maghemite Particles. *J. Colloid Interface Sci.* **2003**, *265*, 283–295.
49. Pasche, S.; De Paul, S. M.; Vörös, J.; Spencer, N. D.; Textor, M. Poly(L-lysine)-graft-poly(ethylene glycol) Assembled Monolayers on Niobium Oxide Surfaces: A Quantitative Study of the Influence of Polymer Interfacial Architecture on Resistance to Protein Adsorption by ToF-SIMS and *In Situ* OWLS. *Langmuir* **2003**, *19*, 9216–9225.
50. Konradi, R.; Acikgoz, C.; Textor, M. Polyoxazolines for Nonfouling Surface Coatings—A Direct Comparison to the Gold Standard PEG. *Macromol. Rapid Commun.* **2012**, *33*, 1663–1676.
51. Feuz, L. On the Conformation of Graft-Copolymers with Polyelectrolyte Backbone in Solution and Adsorbed on Surfaces. PhD Thesis, ETH Zürich, 2006.
52. Müller, M. T.; Yan, X.; Lee, S.; Perry, S. S.; Spencer, N. D. Lubrication Properties of a Brushlike Copolymer as a Function of the Amount of Solvent Absorbed within the Brush. *Macromolecules* **2005**, *38*, 5706–5713.
53. Amstad, E.; Zürcher, S.; Mashaghi, A.; Wong, J. Y.; Textor, M.; Reimhult, E. Surface Functionalization of Single Superparamagnetic Iron Oxide Nanoparticles for Targeted Magnetic Resonance Imaging. *Small* **2009**, *5*, 1334–1342.
54. Li, W.; Zhang, A.; Schlüter, A. D. Thermoresponsive Dendronized Polymers with Tunable Lower Critical Solution Temperatures. *Chem. Commun.* **2008**, 5523–5525.
55. Hawker, C. J.; Farrington, P. J.; Mackay, M. E.; Wooley, K. L.; Fréchet, J. M. J. Molecular Ball Bearings: The Unusual Melt Viscosity Behavior of Dendritic Macromolecules. *J. Am. Chem. Soc.* **1995**, *117*, 4409–4410.
56. Tomalia, D. A.; Fréchet, J. M. J. Introduction to the Dendritic State. *Dendrimers and Other Dendritic Polymers*; John Wiley & Sons, Ltd: New York, 2002; pp 1−44.
57. Li, W.; Zhang, A.; Feldman, K.; Walde, P.; Schlüter, A. D. Thermoresponsive Dendronized Polymers. *Macromolecules* **2008**, *41*, 3659–3667.
58. Lutz, J.-F.; Akdemir, Ö.; Hoth, A. Point by Point Comparison of Two Thermosensitive Polymers Exhibiting a Similar LCST: Is the Age of Poly(NIPAM) Over?. *J. Am. Chem. Soc.* **2006**, *128*, 13046–13047.
59. Junk, M. J. N.; Li, W.; Schlüter, A. D.; Wegner, G.; Spiess, H. W.; Zhang, A.; Hinderberger, D. EPR Spectroscopic Characterization of Local Nanoscopic Heterogeneities during the Thermal Collapse of Thermoresponsive Dendronized Polymers. *Angew. Chem., Int. Ed.* **2010**, *49*, 5683–5687.
60. Junk, M. J. N.; Li, W.; Schlüter, A. D.; Wegner, G.; Spiess, H. W.; Zhang, A.; Hinderberger, D. EPR Spectroscopy Provides a Molecular View on Thermoresponsive Dendronized Polymers below the Critical Temperature. *Macromol. Chem. Phys.* **2011**, *212*, 1229–1235.
61. Linert, W.; Jameson, R. F.; Herlinger, E. Complex Formation Followed by Internal Electron Transfer: The Reaction between L-Dopa and Iron(III). *Inorg. Chim. Acta* **1991**, *187*, 239–247.
62. Lee, H.; Scherer, N. F.; Messersmith, P. B. Single-Molecule Mechanics of Mussel Adhesion. *Proc. Natl. Acad. Sci. U.S.A.* **2006**, *103*, 12999–13003.
63. Shultz, M. D.; Reveles, J. U.; Khanna, S. N.; Carpenter, E. E. Reactive Nature of Dopamine as a Surface Functionalization Agent in Iron Oxide Nanoparticles. *J. Am. Chem. Soc.* **2007**, *129*, 2482–2487.
64. Jeon, S. I.; Lee, J. H.; Andrade, J. D.; De Gennes, P. G. Protein−Surface Interactions in the Presence of Polyethylene Oxide: I. Simplified Theory. *J. Colloid Interface Sci.* **1991**, *142*, 149–158.
65. McPherson, T.; Kidane, A.; Szleifer, I.; Park, K. Prevention of Protein Adsorption by Tethered Poly(ethylene oxide) Layers: Experiments and Single-Chain Mean-Field Analysis. *Langmuir* **1998**, *14*, 176–186.
66. Kahani, S. A.; Jafari, M. A New Method for Preparation of Magnetite from Iron Oxyhydroxide or Iron Oxide and Ferrous Salt in Aqueous Solution. *J. Magn. Magn. Mater.* **2009**, *321*, 1951–1954.

67. Lide, D. R. *Handbook of Chemistry and Physics*, 75th ed.; CRC Press, Inc.: Boca Raton, FL, 1994.
68. Hilfiker, J. N.; Synowicki, R. A. Spectroscopic Ellipsometry for Polymer Thin Films. *Solid State Technol.* **1998**, *41*, 101–110.
69. MSDS Oleylamine, Sigma-Aldrich, **2010**.